ACS OMEGA

Open Access

http://pubs.acs.org/journal/acsodf

Article

Metastructure Engineering with Ruddlesden–Popper 2D Perovskites: Stability, Flexibility, and Quality Factor Trade-Offs

Seyedeh Bita Saadatmand,[§] Samad Shokouhi,[§] Vahid Ahmadi,* and Seyedeh Mehri Hamidi

Cite This: *ACS Omega* 2024, 9, 24925−24932

Read Online

ACCESS | Metrics & More | Article Recommendations | Supporting Information

ABSTRACT: In this study, we investigate the opto-electro-mechanical properties, thermodynamic stability, and moisture stability of the Ruddlesden–Popper (RP) two-dimensional perovskites of L_2PbI_4 (L = PEA, FPEA, BA, and BZA) using density functional theory. The goal is to explore their potential application in metastructures. The results show that the stability of $FPEA_2PbI_4$ is better than that of PEA_2PbI_4, BA_2PbI_4, and BZA_2PbI_4 due to the replacement of a hydrogen atom with a fluorine atom. On the other hand, BA_2PbI_4 is more flexible than other materials because it lacks an aromatic ring in its spacer cation, but it is less stable. We introduce a new kind of metastructure composed of an RP perovskite film and conduct an extensive investigation of the quasi-bound states in the continuum (q-BIC) characteristics by near-field analysis and multipole decomposition calculations. The q-BIC resonances in BZA_2PBI_4 have a greater quality factor due to its larger refractive index in comparison to other materials. Therefore, based on these results, the perovskite materials can be selected for the metastructures from different aspects of stability, flexibility, and refractive index.

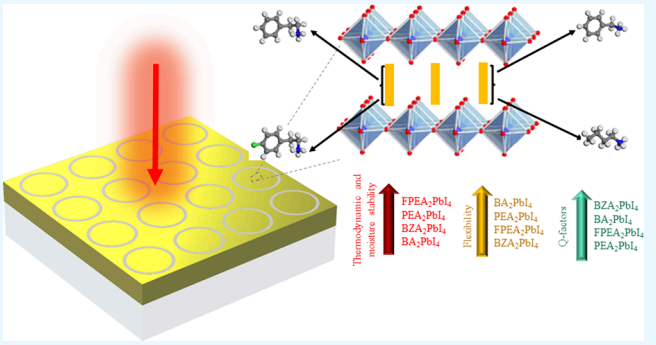

1. INTRODUCTION

The terahertz (THz) potential for various applications, particularly in sensor technology, has been hindered by its weak interaction with materials, resulting in limited progress in this field.[1] An effective solution to overcome this challenge is to use the bound state in the continuum (BIC) concept in metasurfaces. The symmetry-protected bound state in the continuum (sp-BIC) occurs when the eigenmodes of the periodic structure cannot couple with the incident wave due to symmetry mismatch.[2] By breaking the symmetry, these modes can be converted into quasi-BIC (q-BIC) states, which have a high-quality factor (*Q*-factor) and can significantly enhance the interaction between matter and light.[3] To enhance the interaction of light and matter through metasurfaces, it is essential to use materials that have two key characteristics: a high refractive index and near-zero loss. Only a few materials have these properties in the THz range. Silicon and lithium tantalate are commonly used in dielectric metasurfaces due to their desirable characteristics.[4,5] However, despite some progress in the THz region, it is essential to investigate new materials.

The Ruddlesden–Popper (RP) two-dimensional (2D) perovskites are widely used in optoelectronic fields due to their remarkable structural, electrical, optical, and mechanical properties, such as cost-effectiveness, simple fabrication, interesting nonlinear effects, tunable bandgap, and flexibility. The general formula for these materials is L_2BX_4, where L, B, and X are monovalent spacer cation, metal cation, and halide anion, respectively. The L is usually aliphatic alkylammonium (such as butylammonium (BA)) and aromatic alkylammonium (such as pehenthylammonium (PEA), fluorophenthylammonium (FPEA), and benzylammonium (BZA)).[6] The aliphatic spacer cation consists of ammonium and carbon chains, but in the aromatic cation, there is an aromatic ring at the end of the cation. The change of L impacts the different properties of 2D perovskite, causing a variation in the bond angle of the inorganic part of perovskite and, as a result, changes in the values of bandgap energy and refractive index.[7] Also, changing the L causes an alteration in the stability and flexibility of the perovskite material. A few cases regarding the effect of changing the L cation, as well as the study of some properties of 2D perovskites, have already been investigated. Recently, perovskites have been utilized in sensing and solar cell applications.[8−12] Slavney et al. demonstrated experimentally that FPEA is more stable compared to PEA.[13] In another study, Tu et al. performed a comparison of the mechanical

Received: February 25, 2024
Revised: May 11, 2024
Accepted: May 15, 2024
Published: May 29, 2024

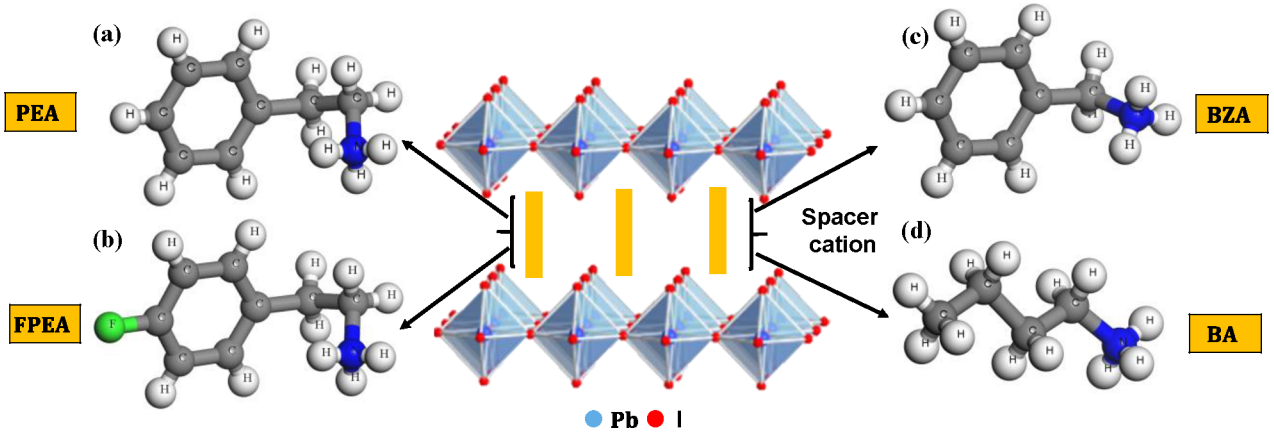

Figure 1. Schematic structure of (a) PEA, (b) FPEA, (c) BZA, and (d) BA as spacer cations in RP 2D perovskites.

Table 1. Crystal Data and Structure for the Proposed Materials

2D perovskite	lattice parameters	space group
PEA_2PbI_4[20]	a = 8.876 Å, b = 8.737 Å, c = 16.655 Å, α = 94.29°, β = 99.78°, γ = 90.34° (experiment); a = 8.796 Å, b = 8.618 Å, c = 17.318 Å, α = 95.18°, β = 102.34°, γ = 90.16° (optimized PBE)	triclinic $P1$
$FPEA_2PbI_4$[21]	a = 16.735 Å, b = 8.626 Å, c = 8.801 Å, α = 90°, β = 98.67°, γ = 90° (experiment); a = 16.718 Å, b = 8.668 Å, c = 8.803 Å, α = 90°, β = 99.967°, γ = 90° (optimized PBE)	monoclinic $P2_1/c$
BA_2PbI_4[22]	a = 8.863 Å, b = 8.682 Å, c = 27.570 Å, $\alpha = \beta = \gamma$ = 90° (experiment); a= 8.892 Å, b = 8.656 Å, c = 28.565 Å, $\alpha = \beta = \gamma$ = 90° (optimized PBE)	orthorhombic $PBCA$
BZA_2PbI_4[23]	a = 9.162 Å, b = 8.689 Å, c = 28.780 Å, $\alpha = \beta = \gamma$ = 90° (experiment); a = 9.237 Å, b = 8.650 Å, c = 28.752 Å, $\alpha = \beta = \gamma$ = 90° (optimized PBE)	orthorhombic $PBCA$

properties of 2D perovskites, namely, BA_2PbI_4 and PEA_2PbI_4.[14] In addition, the optical and electrical properties of BA_2PbI_4 and PEA_2PbI_4 were studied through density functional theory (DFT) calculations and experimentally by Ghosh et al.[15] The electrical and mechanical properties of BZA_2PbI_4 were also presented through DFT calculations.[16,17] Therefore, it is necessary to comprehensively study the properties of RP 2D perovskites and compare them based on the L cation variations.

In this study, we utilize DFT analysis to explore the mechanical, optical, electrical, and stability characteristics of L_2PbI_4 (L = PEA, FPEA, BA, and BZA). We aim to investigate their potential suitability for THz applications and compare them in detail, which have not been reported so far, to the best of our knowledge. The results reveal that $FPEA_2PbI_4$ exhibited higher thermodynamic and moisture stability compared to PEA_2PbI_4, BA_2PbI_4, and BZA_2PbI_4. Furthermore, the highest refractive index is observed in BZA_2PbI_4. The elastic moduli calculated from the Voigt−Reuss−Hill (VRH) approximations indicate that these compounds possess mechanical stability and flexibility, with BA_2PbI_4 demonstrating the highest flexibility. These findings demonstrate the noteworthy characteristics of these materials, including thermodynamic and moisture stability, ductility, flexibility, a high dielectric constant, and zero loss in the THz range. We introduce a novel kind of metastructure composed of a new RP 2D perovskite film. We follow our design presented in ref 18. By breaking the symmetry of the structure, the multidark modes (BICs) of the structure, which depend on the polarization of the incident wave, are transformed into bright modes (q-BICs) with an ultrahigh-quality factor. This study provides a valuable reference for the development of applications in the THz region, such as bidirectional switches, multichannel wearable sensors, optical tweezers, and filters.

2. MATERIALS AND METHODS

The general formula for RP 2D perovskites is L_2BX_4, where L represents a monovalent spacer cation, and there is a van der Waals force between the two cations (L_2). Two important types of spacer cations used in RP 2D perovskites are aromatic and aliphatic alkylammonium. The general formula for aromatic alkylammonium spacer cations is $Y\text{-}(CH_2)_nNH_3$, where Y is the aromatic ring and $(CH_2)_n$ represents the carbon chain.[19] The general formula for aliphatic alkylammonium spacer cations is $C_nH_{2n+1}NH_3$, where C_nH_{2n+1} is the carbon chain. In both types, NH_3 at the end section of the spacer cation is the ammonium unit of organic groups that binds to the metal halide layer (PbI_4) through hydrogen bonding.[7]

Phenethylammonium (PEA) is an aromatic spacer cation with n = 2 in the general formula ($C_6H_5C_2H_4NH_3$), as shown in Figure 1a. The fluorophenethylammonium (FPEA) aromatic spacer cation, illustrated in Figure 1b, is obtained by replacing one hydrogen (H) atom in the aromatic ring section of the cation with a fluorine (F) atom. Benzylammonium (BZA), with n = 1 in the general formula $C_6H_5CH_2NH_3$, is presented in Figure 1c. Comparing the schematic of the two cations, BZA and PEA, the difference lies in the carbon chain length. Another spacer cation, butylammonium (BA), an aliphatic spacer cation with n = 4 in the general formula $C_4H_9NH_3$, is depicted in Figure 1d.

The crystal structures of the proposed 2D perovskite materials, i.e., PEA_2PbI_4, $FPEA_2PbI_4$, BA_2PbI_4, and BZA_2PbI_4, are presented in Figure S1. Table 1 displays the experimental and optimized lattice parameters using the Broyden−Fletcher−Goldfarb−Shanno (BFGS) algorithm and crystal phase of these materials at room temperature. According to this table, BA_2PbI_4 and BZA_2PbI_4 both exhibit an orthorhombic phase, while PEA_2PbI_4 and $FPEA_2PbI_4$ have triclinic and monoclinic phases, respectively. The description of DFT calculations can be found in Section S1.

https://doi.org/10.1021/acsomega.4c01827
ACS Omega 2024, 9, 24925−24932

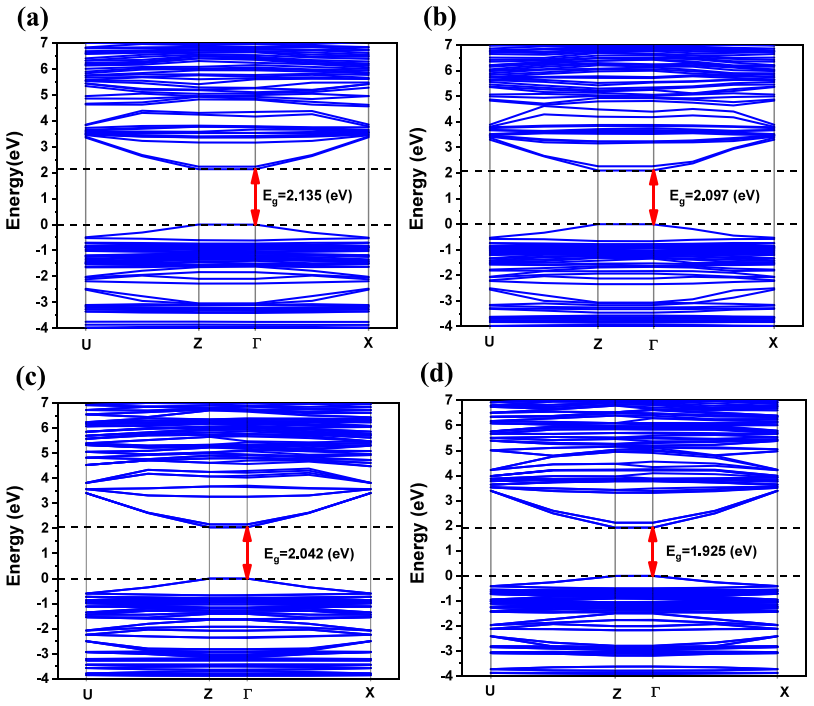

Figure 2. Band structure and bandgap energy of (a) PEA_2PbI_4, (b) $FPEA_2PbI_4$, (c) BA_2PbI_4, and (d) BZA_2PbI_4.

3. RESULTS AND DISCUSSION

3.1. Electronic Properties. The organic spacer (L) can influence the bandgap energy (E_g) of the 2D perovskite materials through structural distortion. The average Pb−I−Pb bond angle indicates octahedral tilting in the inorganic section of the 2D perovskite. Reducing the bond angle due to decreased structural symmetry distorts the interaction between the Pb s-orbitals and I p-orbitals in the valence band maximum (VBM).[7] As a result, the E_g value increases (see Section S2). Using the DFT analysis, we achieve the average Pb−I−Pb bond angle values of 157.565°, 155.018°, 152.984°, and 152.262° for BZA_2PbI_4, BA_2PbI_4, $FPEA_2PbI_4$, and PEA_2PbI_4, respectively (see Figure S3 and Table S1). The band structure and E_g values resulting from DFT calculations are illustrated in Figure 2. The E_g values for PEA_2PbI_4, $FPEA_2PbI_4$, BA_2PbI_4, and BZA_2PbI_4 are 2.135, 2.097, 2.042, and 1.925 eV, respectively. The results depicted in Figure 2 reveal that the bandgap increases with the average Pb−I−Pb bond angle decreasing.

Sheikh et al.[24] conducted DFT calculations for PEA_2PbI_4 perovskite, while Varghese et al.[25] performed similar calculations for BA_2PbI_4 perovskite using the Vienna Ab initio Simulation Package (VASP). In their work, they derived the value of E_g utilizing the Perdew−Burke−Ernzerhof (PBE) exchange-correlation function, with a k-point grid of 5 × 5 × 1 and an energy cutoff of 500 eV. Table 2 compares our results with their simulation results as well as experimental data. It shows that the data are very close together.

Table 2. Comparison of Our Results with Other Findings for E_g

2D perovskite	our results (PBE)	our results (HSE06)	other results (PBE)	other results (experimental)
PEA_2PbI_4	2.135	2.334	2.13[24]	2.38,[21] 2.35[24]
$FPEA_2PbI_4$	2.097	2.321		2.37[21]
BA_2PbI_4	2.042	2.218	2.08[25]	2.25[26]
BZA_2PbI_4	1.925	2.174		2.18[17]

3.2. Optical Properties. The complex refractive index (RI) of L_2PbI_4 (L = PEA, FPEA, BA, and BZA) perovskites is shown in Figure 3. The results show that the real part of the RI of these materials in the THz range is higher than 2, while the imaginary part remains at zero. Specifically, the real parts of the RI at zero frequency for PEA_2PbI_4, $FPEA_2PbI_4$, BA_2PbI_4, and BZA_2PbI_4 are 2.100, 2.102, 2.104, and 2.184, respectively. These values exhibit a reverse trend with respect to the corresponding E_g values. When the F atom in the FPEA cation replaces H in PEA, the charge on the aromatic ring side becomes more negative, while the charge on the NH_3 side becomes more positive. As a result of charge redistribution in FPEA, the dipole moment and dielectric constant increase.[27] Consequently, the RI of FPEA is greater than that of PEA. Furthermore, considering the difference in Pb−I−Pb bond angles mentioned above and their effect on E_g values, it can be observed that BZA_2PbI_4 exhibits the highest RI, whereas PEA_2PbI_4 shows the lowest among the proposed materials.

3.3. Mechanical Properties. The mechanical stability of 2D perovskite materials, i.e., L_2PbI_4 (L = PEA, FPEA, BA, and BZA), is investigated based on the elastic constants and crystal phases of these materials. The mechanical stability in triclinic and monoclinic phases is studied through the conditions presented in eqs S19−S22. Similarly, for the orthorhombic phase, the conditions of eqs S23−S25 should be satisfied. Table S2 displays the elastic constants obtained for the proposed materials through DFT calculations. We can observe that the proposed structures exhibit mechanical stability.

Utilizing elastic constants presented in Table S2 and applying VRH approximations, we derive the mechanical properties of L_2PbI_4 (L = PEA, FPEA, BA, and BZA) perovskites including Poisson's ratio, Pugh's ratio, bulk

https://doi.org/10.1021/acsomega.4c01827
ACS Omega 2024, 9, 24925−24932

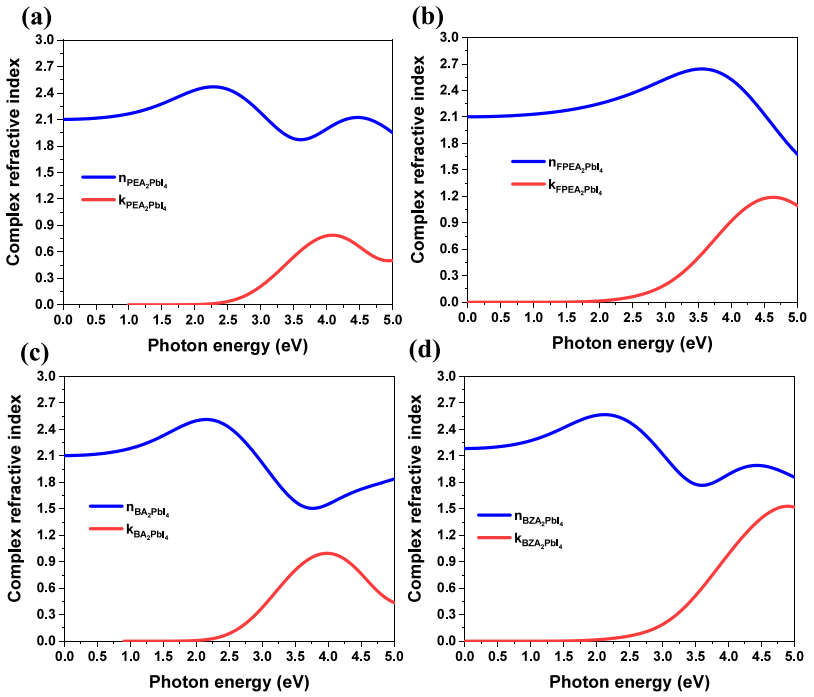

Figure 3. Complex refractive index of (a) PEA_2PbI_4, (b) $FPEA_2PbI_4$, (c) BA_2PbI_4, and (d) BZA_2PbI_4.

Table 3. Mechanical Properties of L_2PbI_4 (L = PEA, FPEA, BA, and BZA)

2D perovskite		PEA_2PbI_4	$FPEA_2PbI_4$	BA_2PbI_4	BZA_2PbI_4
Voigt	B_V (GPa)	12.024	13.675	11.513	12.704
	G_V (GPa)	7.050	7.031	4.796	6.404
	E_V (GPa)	17.692	18.008	12.635	16.454
	B_V/G_V	1.705	1.940	2.400	1.959
	ν_V	0.254	0.280	0.317	0.284
Reuss	B_R (GPa)	11.354	13.402	11.428	12.406
	G_R (GPa)	5.437	6.373	4.223	6.191
	E_R (GPa)	14.146	16.503	11.279	15.925
	B_R/G_R	2.074	2.10	2.706	2.003
	ν_R	0.292	0.294	0.335	0.286
Hill	B_H (GPa)	11.689	13.539	11.470	12.555
	G_H (GPa)	6.261	6.702	4.509	6.298
	E_H (GPa)	15.939	17.259	11.957	16.189
	B_H/G_H	1.866	2.010	2.543	1.981
	ν_H	0.272	0.287	0.326	0.285
	type of material	ductile	ductile	ductile	ductile

Table 4. Formation Enthalpy Energy and Water Molecule Adsorption Energy of L_2PbI_4 (L = PEA, FPEA, BA, and BZA)

2D perovskite	FE (eV)	E_{ads} (eV)
PEA_2PbI_4	−4.689	−0.146
$FPEA_2PbI_4$	−4.825	−0.135
BA_2PbI_4	−3.015	−0.207
BZA_2PbI_4	−3.115	−0.199

modulus, Young's modulus, and shear modulus. The corresponding results from DFT analysis are listed in Table 3.

Table 3 shows that changing the spacer cation (L) affects the mechanical properties. These results can be explained as follows: (a) For aromatic spacer cations, increasing the length of the carbon chain (or the number of carbon atoms) makes the material more flexible.[28] Therefore, PEA (with C_2H_4) has smaller modulus coefficients than BZA (with CH_2), indicating its greater flexibility. (b) Although the length of the PEA cation (aromatic type) is longer than that of the BA cation (aliphatic type), the BA cation is more flexible than the PEA cation. This is because of the presence of a rigid aromatic ring in PEA. The CH···π interaction in PEA is stiffer than the CH_3−CH_3 interaction in BA, which agrees well with ref 14 in which Young's modulus value of BA_2PbI_4 is lower than that of PEA_2PbI_4. (c) In aromatic cations, replacing H with F leads to a redistribution of electron density, resulting in a stronger π−π interaction. This makes the material stiffer. Consequently, FPEA has higher modulus coefficients and less flexibility than PEA. Therefore, BA_2PbI_4 is the most flexible among the proposed materials, whereas BZA_2PbI_4 has less flexibility compared to the others.

3.4. Stability. We calculate the thermodynamic and moisture stability of the proposed materials. To assess moisture stability, we consider six different cases (see Section S4). Based on the results of Table 4, we can conclude that (a) the greater stability of PEA_2PbI_4 compared to BA_2PbI_4 can be attributed to the presence of an aromatic ring, which causes a larger spacer length. (b) PEA_2PbI_4 is more stable than BZA_2PbI_4 because of the longer carbon chain (or higher number of carbon atoms). (c) $FPEA_2PbI_4$ is more stable than PEA_2PbI_4 due to the replacement of a H atom with a F atom. This substitution not only strengthens the covalent bond of the spacer cation but also enhances the hydrogen bonding between the ammonium part with the inorganic layer, resulting in increased stability.[29] In addition, the atomic radius of the F atom is larger than that of the H atom, which leads to a greater spacer cation length in FPEA and enhances the stability. Moreover, the aromatic phenyl−phenyl (π−π) stacking in $FPEA_2PbI_4$ is stronger compared to PEA_2PbI_4. The results obtained indicate that the FPEA spacer cation exhibits greater stability compared to PEA.

https://doi.org/10.1021/acsomega.4c01827
ACS Omega 2024, 9, 24925−24932

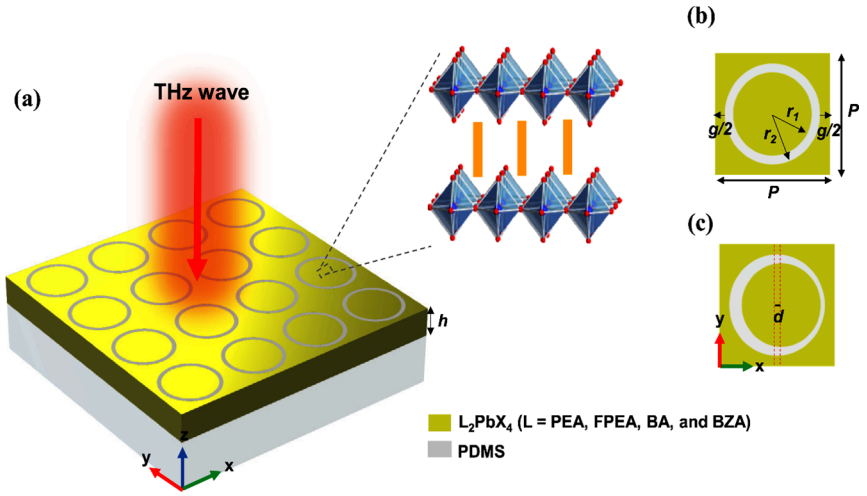

Figure 4. (a) Schematic of the suggested design, (b) symmetric unit cell, and (c) asymmetric unit cell.

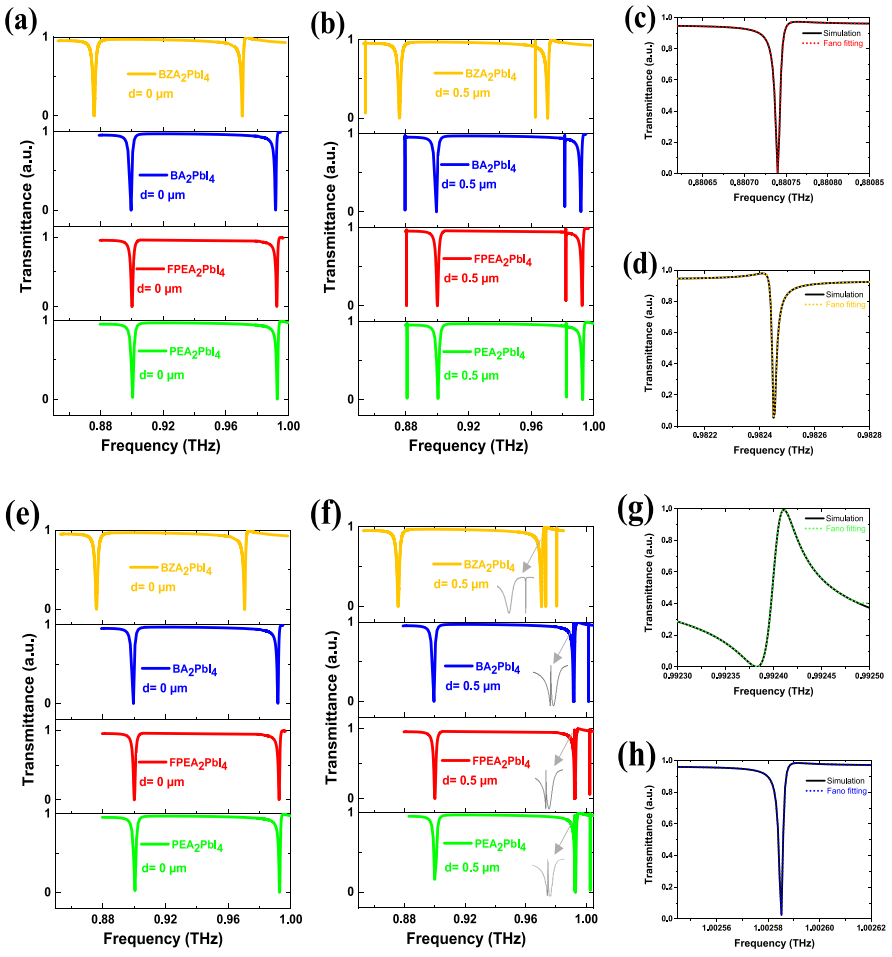

Figure 5. (a) Transmittance spectrum under *y*-polarization for the symmetry structure, (b) transmittance spectrum under *y*-polarization for asymmetry structure, (c) Fano fitting of mode A_2 in PEA_2PbI_4 for d = 0.5, (d) Fano fitting of mode B_2 in PEA_2PbI_4 for d = 0.5, (e) transmittance spectrum under *x*-polarization for the symmetry structure, (f) transmittance spectrum under *x*-polarization for the asymmetry structure, (g) Fano fitting of mode A_1 in PEA_2PbI_4 for d = 0.5, and (h) Fano fitting of mode B_1 in PEA_2PbI_4 for d = 0.5.

Based on the results, the proposed 2D perovskites exhibit high thermodynamic, moisture, mechanical stability, and flexibility. They also have a high RI and zero losses in the THz region. Consequently, these materials are ideal to be employed in BIC-based metastructures in this range.

3.5. Application in the BIC Metastructure. Here, we proposed a metastructure with multiple functionalities based on the suggested 2D perovskites, with the schematic structure illustrated in Figure 4. We follow the design presented in ref 18. The suggested metastructure consists of a PDMS substrate with a refractive index of 1.4, along with a thin layer of 2D

https://doi.org/10.1021/acsomega.4c01827
ACS Omega 2024, 9, 24925−24932

Table 5. Q-Factors of q-BICs for the Proposed 2D Materials

2D perovskite	Q-factors of A_1	Q-factors of B_1	Q-factors of A_2	Q-factors of B_2
PEA_2PbI_4	1.2×10^4	5×10^5	4.7×10^5	4×10^4
$FPEA_2PbI_4$	1.23×10^4	5.2×10^5	4.88×10^5	4.21×10^4
BA_2PbI_4	1.27×10^4	5.46×10^5	5.19×10^5	4.52×10^4
BZA_2PbI_4	1.7×10^4	6.3×10^5	6.1×10^5	5.65×10^4

perovskite on its surface. The 2D perovskite structure is highlighted in Figure 4a. This perovskite layer features a regular arrangement of slot rings, as shown in Figure 4a. The symmetric and asymmetric unit cells are shown in Figure 4b,c, respectively, each distinguished by specific structural characteristics, including the inner and outer radii of the rings (r_1 = 67.5 μm and r_2 = 75 μm), the gap between neighboring rings (g = 31.25 μm), the thickness of the perovskite layer (h = 72.5 μm), and the unit cell's periodicity (P = 181.25 μm). By adjusting the position of the inner ring away from the center, we can create an asymmetric configuration denoted by the offset distance d. To assess the optical properties of the metastructure, we utilize the finite element method. The simulation applies Floquet−Bloch periodic boundary conditions along the x−z and y−z planes. Furthermore, two perfectly matched layers are placed along the z-axis. These layers are supported by scattering boundary conditions.

When d is zero, the structure exhibits C_{4v} symmetry. The transmittance spectra for y and x polarizations are shown in Figure 5a,e, respectively. Two bright modes are observed for both polarizations. These modes have the same frequencies under both x and y polarizations, indicating their degeneracy. In addition, there are two dark modes (BICs) in the transmittance spectrum for each polarization. These modes are pure BICs at d equal zero, which means that there is no out-coupling from the dark states to the zero-order channel. By introducing an offset, it becomes possible for q-BICs to be selectively achieved depending on the polarization of the incident waves (Figure 5b,f). Modes A_1 and B_1 emerge in the x polarization of the incident wave, whereas modes A_2 and B_2 appear in the y polarization of the incident wave. Furthermore, as d deviates from zero, the resonance peaks of q-BIC become broader (see Figure S5). The results in Figure 5a,b,e,f indicate that there is a redshift in the BIC frequencies when the dielectric coefficient of the 2D perovskites increases. For

Table 6. Summary of the Key Properties of the Proposed Materials

Thermodynamic and moisture stability	Flexibility	Q-factors
$FPEA_2PbI_4$	BA_2PbI_4	BZA_2PbI_4
PEA_2PbI_4	PEA_2PbI_4	BA_2PbI_4
BZA_2PbI_4	$FPEA_2PbI_4$	$FPEA_2PbI_4$
BA_2PbI_4	BZA_2PbI_4	PEA_2PbI_4

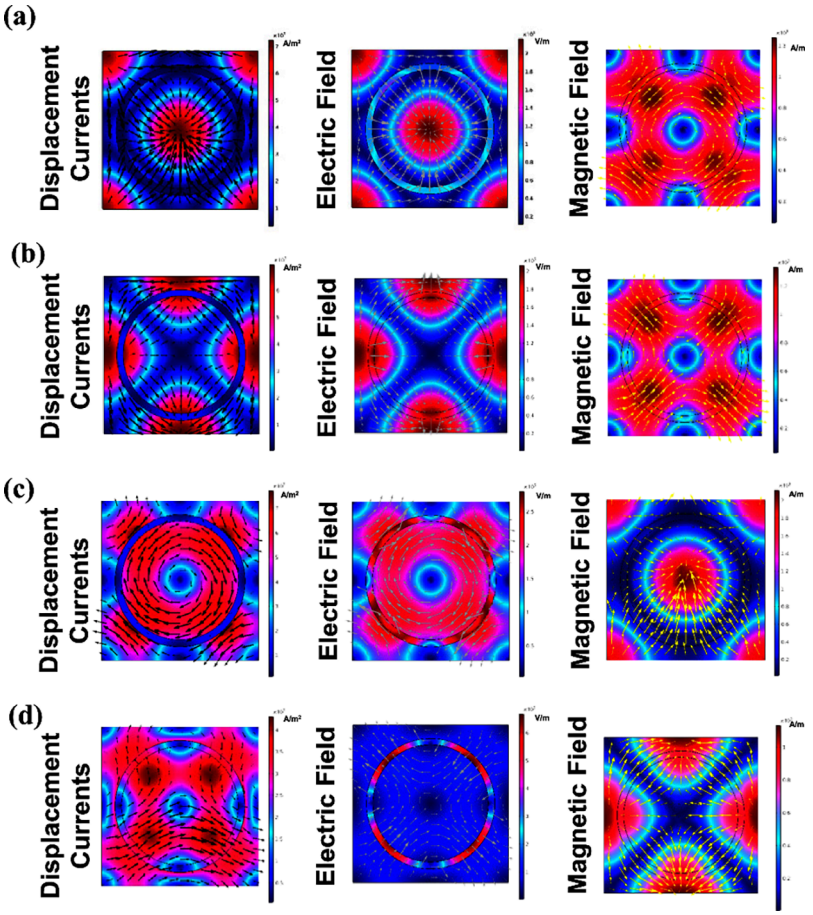

Figure 6. Color maps of displacement currents, electric and magnetic fields, and vector distributions in the x−y plane for (a) A_1, (b) B_1, (c) A_2, and (d) B_2.

https://doi.org/10.1021/acsomega.4c01827
ACS Omega 2024, 9, 24925−24932

example, BZA_2PbI_4 with the higher dielectric coefficient has a larger redshift than the others. The redshift can be explained by perturbation theory as $(\delta\omega/\omega_0) = -(\iiint \Delta\varepsilon|E|^2 dV/2 \iiint \varepsilon_0|E|^2 dV)$, where $\delta\omega$, ω_0, and $\Delta\varepsilon$ represent the resonance shift, resonance frequency, and change in the dielectric coefficient, respectively.[30] Increasing the dielectric coefficient of the materials results in a larger redshift of the resonances. To fit the Fano resonance curves of q-BICs, the Fano formula, $T_{\text{Fano}}(\omega) = |a_1 + ja_2 + \frac{b}{\omega - \omega_0 + j\gamma}|^2$, is used.[31] In this equation, ω_0 represents the resonance frequency, a_1, a_2, and b are constants, and γ represents the total damping rate that characterizes the Q-factor ($Q = \omega_0/2\gamma$) of the q-BICs. Figure 5c,d,g,h illustrates the fitting results for the four q-BICs for PEA_2PbI_2. The Q-factors of the proposed materials for d equal to 0.5 μm are presented in Table 5. The results indicate that the q-BICs in BZA_2PbI_4 have higher Q-factors than those of the other proposed materials due to its higher dielectric coefficient in the THz region. On the opposite, the q-BICs in PEA_2PbI_4, which has a lower dielectric coefficient than the other proposed materials, exhibit lower Q-factors. Consequently, metasurfaces composed of the suggested 2D materials show promising potential in various applications such as filters, bidirectional optical switches, optical tweezers, and tunable and flexible sensors (for example, a bidirectional optical switch is presented in Section S6).

To investigate the characteristics of the resonances, we analyze the distribution of displacement current, electric field, and magnetic field illustrated in Figure 6. In mode A_1, the arrangement of magnetic moments is in a circular shape (Figure 6a). The existence of current loops in the perpendicular plane indicates the occurrence of the magnetic toroidal dipole mode. Mode B_1 displays nonparallel magnetic moments, signifying a magnetic quadrupole (Figure 6b). In mode A_2, the field map has a vortex pattern generated by displacement currents flowing through the inner ring (Figure 6c). Furthermore, the magnetic moments adopt a vortex formation within the plane perpendicular to the current. This configuration corresponds to an electric toroidal dipole. Last, in mode B_2 shown in Figure 6d, the presence of opposing electric moments allows for the appearance of an electric quadrupole mode. The results of the multipole decomposition are shown in Section S7.

In Table 6, the proposed materials are arranged according to the three characteristics of stability, flexibility, and Q-factor. The results indicate that $FPEA_2PbI_4$ offers the highest stability, BA_2PbI_4 provides the greatest flexibility, and BZA_2PbI_4 exhibits the highest Q-factor. Therefore, there are trade-offs between the thermodynamic and moisture stability, flexibility, and Q-factor within the proposed materials. Accordingly, depending on specific requirements, it is possible to choose the suitable material to be employed in the metastructure.

4. CONCLUSIONS

In summary, we first used DFT calculations to determine various properties of 2D perovskites L_2PbI_4 (L = PEA, FPEA, BA, and BZA), including bond angle, bandgap energy, refractive index, elastic constants, coefficients of mechanical modulus, and moisture and thermodynamic stability. Our analysis revealed that BA_2PbI_4 is the most flexible among these four materials due to the absence of an aromatic ring, while $FPEA_2PbI_4$, which contains an aromatic ring and a fluorine atom, is the most stable material. We then presented a novel type of metastructure that utilizes a Ruddlesden–Popper perovskite film and conducted a thorough investigation of its q-BIC properties using the finite element method. Our findings indicated that the q-BIC resonances in BZA_2PBI_4 exhibited a higher Q-factor compared to other materials, which can be attributed to its larger refractive index. Based on these results, one can choose the desired material for metastructures based on better stability, flexibility, and higher Q-factor.

■ ASSOCIATED CONTENT

Supporting Information

The Supporting Information is available free of charge at https://pubs.acs.org/doi/10.1021/acsomega.4c01827.

Section S1: details of DFT computational methods; Section S2: Pb–I–Pb bond angles; Section S3: mechanical properties; Section S4: moisture stability; Section S5: Q-factor of the q-BICs; Section S6: application of the BIC metastructure; Section S7: multipole decomposition (PDF)

■ AUTHOR INFORMATION

Corresponding Author

Vahid Ahmadi − *Faculty of Electrical and Computer Engineering, Tarbiat Modares University, Tehran 14115-194, Iran;* orcid.org/0000-0002-4131-2153; Email: v_ahmadi@modares.ac.ir

Authors

Seyedeh Bita Saadatmand − *Faculty of Electrical and Computer Engineering, Tarbiat Modares University, Tehran 14115-194, Iran*

Samad Shokouhi − *Faculty of Electrical and Computer Engineering, Tarbiat Modares University, Tehran 14115-194, Iran*

Seyedeh Mehri Hamidi − *Magneto-plasmonic Lab, Laser and Plasma Research Institute, Shahid Beheshti University, Tehran 14115-194, Iran;* orcid.org/0000-0002-5298-2224

Complete contact information is available at: https://pubs.acs.org/10.1021/acsomega.4c01827

Author Contributions

[§]S.B.S. and S.S. contributed equally to this work.

Author Contributions

The manuscript was written through the contributions of all authors. All authors have given approval to the final version of the manuscript.

Notes

The authors declare no competing financial interest.

■ ACKNOWLEDGMENTS

The authors would like to thank Mr. Mahmood Sadeghi for his assistance.

■ REFERENCES

(1) Fischer, B. M.; et al. Terahertz time-domain spectroscopy and imaging of artificial RNA. *Opt. Express* **2005**, *13* (14), 5205–5215.

(2) Han, S.; et al. Extended bound states in the continuum with symmetry-broken terahertz dielectric metasurfaces. *Adv. Opt. Mater.* **2021**, *9* (7), No. 2002001.

(3) Doeleman, H. M.; et al. Experimental observation of a polarization vortex at an optical bound state in the continuum. *Nat. Photonics* **2018**, *12* (7), 397−401.
(4) Wang, P.; et al. Ultra-high-Q resonances in terahertz all-silicon metasurfaces based on bound states in the continuum. *Photonics Research* **2022**, *10* (12), 2743−2750.
(5) Wang, Y.; et al. Ultrasensitive terahertz sensing with high-Q toroidal dipole resonance governed by bound states in the continuum in all-dielectric metasurface. *Nanophotonics* **2021**, *10* (4), 1295−1307.
(6) Shokouhi, S; Saadatmand, S. B.; Ahmadi, V.First Principles Study of Optical and Electrical Properties for Mixed-halide 2D BA2PbBr4-xClx (x= 0, 2, and 4) as an Active Layer of Perovskite Light Emitting Diode. In *2023 5th Iranian International Conference on Microelectronics (IICM)*, pp 219−221, IEEE, 2023.
(7) Paritmongkol, W.; et al. Synthetic variation and structural trends in layered two-dimensional alkylammonium lead halide perovskites. *Chem. Mater.* **2019**, *31* (15), 5592−5607.
(8) Chemerkouh, M.J.H.N; Saadatmand, S. B.; Hamidi, S. M. Ultra-high-sensitive biosensor based on SrTiO 3 and two-dimensional materials: Ellipsometric concepts. *Optical Materials Express* **2022**, *12* (7), 2609−2622.
(9) Saadatmand, S. B.; Chemerkouh, M. J. H. N.; Ahmadi, V.; Hamidi, S. M., Design and analysis of highly sensitive plasmonic sensor based on two-dimensional inorganic Ti-MXene and SrTiO 3 interlayer. *IEEE Sensors Journal*, **2023**. DOI: 10.1109/JSEN.2023.3270133
(10) Saadatmand, S. B.; Shokouhi, S.; Hamidi, S. M.; Ahmadi, H.; Babaei, M. Plasmonic heterostructure biosensor based on perovskite/two-dimensional materials. *Optik* **2023**, *290*, No. 171328.
(11) Babaei, M.; Ahmadi, V.; Darvish, G. Opto-electro-mechanical properties of lead-free hybrid double perovskites Cs2AgSbX6 (X= Cl, Br, I) for solar cells: A first-principles study. *J. Phys. Chem. Solids* **2022**, *169*, No. 110880.
(12) Babaei, M.; Ahmadi, V.; Darvish, G. First-principles study of lead-free Ge-based 2D Ruddlesden−Popper hybrid perovskites for solar cell applications. *Phys. Chem. Chem. Phys.* **2022**, *24* (35), 21052−21060.
(13) Slavney, A. H.; et al. Chemical approaches to addressing the instability and toxicity of lead−halide perovskite absorbers. *Inorganic chemistry* **2017**, *56* (1), 46−55.
(14) Tu, Q.; et al. Exploring the factors affecting the mechanical properties of 2D hybrid organic-inorganic perovskites. *ACS Appl. Mater. Interfaces* **2020**, *12* (18), 20440−20447.
(15) Ghosh, D.; et al. Charge carrier dynamics in two-dimensional hybrid perovskites: Dion−Jacobson vs. Ruddlesden−Popper phases. *Journal of Materials Chemistry A* **2020**, *8* (42), 22009−22022.
(16) Gao, H.; et al. Mechanical properties of a 2D lead-halide perovskite, $(C_6H_5CH_2NH_3)_2PbCl_4$, by nanoindentation and first-principles calculations. *J. Phys. Chem. C* **2020**, *124* (35), 19204−19211.
(17) Mao, L.; et al. Role of organic counterion in lead-and tin-based two-dimensional semiconducting iodide perovskites and application in planar solar cells. *Chem. Mater.* **2016**, *28* (21), 7781−7792.
(18) Saadatmand, S. B.; Shokouhi, S.; Ahmadi, V.; Hamidi, S. M. Design and analysis of a flexible Ruddlesden−Popper 2D perovskite metastructure based on symmetry-protected THz-bound states in the continuum. *Sci. Rep.* **2023**, *13* (1), 22411.
(19) Kamminga, M. E.; et al. Confinement effects in low-dimensional lead iodide perovskite hybrids. *Chemistry of materials* **2016**, *28* (13), 4554−4562.
(20) Menahem, M.; et al. Strongly anharmonic octahedral tilting in two-dimensional hybrid halide perovskites. *ACS Nano* **2021**, *15* (6), 10153−10162.
(21) Kikuchi, K.; et al. Structure and optical properties of lead iodide based two-dimensional perovskite compounds containing fluorophenethylamines. *Curr. Appl. Phys.* **2004**, *4* (6), 599−602.
(22) Silver, S.; et al. Characterization of the Valence and Conduction Band Levels of n = 1 2D Perovskites: A Combined Experimental and Theoretical Investigation. *Adv. Energy Mater.* **2018**, *8* (16), No. 1703468.
(23) Du, K. -z.; et al. Two-dimensional lead (II) halide-based hybrid perovskites templated by acene alkylamines: crystal structures, optical properties, and piezoelectricity. *Inorganic chemistry* **2017**, *56* (15), 9291−9302.
(24) Sheikh, M. A. K.; et al. $A_2B_{n-1}Pb_nI_{3n+1}$ (A= BA, PEA; B= MA; n= 1, 2): Engineering Quantum-Well Crystals for High Mass Density and Fast Scintillators. *J. Phys. Chem. C* **2023**, *127* (22), 10737−10747.
(25) Varghese, A.; et al. Near-Infrared and Visible-Range Optoelectronics in 2D Hybrid Perovskite/Transition Metal Dichalcogenide Heterostructures. *Adv. Mater. Interfaces* **2022**, *9* (14), No. 2102174.
(26) Soe, C. M. M.; et al. Structural and thermodynamic limits of layer thickness in 2D halide perovskites. *Proc. Natl. Acad. Sci. U. S. A.* **2019**, *116* (1), 58−66.
(27) Zhao, L.; et al. Influence of Bulky Organo-Ammonium Halide Additive Choice on the Flexibility and Efficiency of Perovskite Light-Emitting Devices. *Adv. Funct. Mater.* **2018**, *28* (31), No. 1802060.
(28) Spanopoulos, I.; et al. Uniaxial expansion of the 2D Ruddlesden−Popper perovskite family for improved environmental stability. *J. Am. Chem. Soc.* **2019**, *141* (13), 5518−5534.
(29) Di, J.; et al. Low trap density para-F substituted 2D PEA_2PbX_4(X= Cl, Br, I) single crystals with tunable optoelectrical properties and high sensitive X-ray detector performance. *Research* **2022**, *2022*, No. 9768019.
(30) Saadatmand, S. B.; Ahmadi, V.; Hamidi, S. M. Quasi-BIC based all-dielectric metasurfaces for ultra-sensitive refractive index and temperature sensing. *Sci. Rep.* **2023**, *13* (1), 20625.
(31) Saadatmand, S. B.; Ahmadi, V.; Hamidi, S. M., December. Resonant field enhancement in all-dielectric metastructures supporting THz bound states in the continuum. In *2022 6th International Conference on Millimeter-Wave and Terahertz Technologies (MMWaTT)* (pp 1−5). IEEE, 2022.

https://doi.org/10.1021/acsomega.4c01827
ACS Omega 2024, 9, 24925−24932